Halide-Driven Synthetic Control of InSb Colloidal Quantum Dots Enables Short-Wave Infrared Photodetectors

Muhammad, Dongsun Choi, Darshan H. Parmar, Benjamin Rehl, Yangning Zhang, Ozan Atan, Gahyeon Kim, Pan Xia, Joao M. Pina, Mengsha Li, Yanjiang Liu, Oleksandr Voznyy, Sjoerd Hoogland, and Edward H. Sargent*

In the III–V family of colloidal quantum dot (CQD) semiconductors, InSb promises access to a wider range of infrared wavelengths compared to many light-sensing material candidates. However, achieving the necessary size, size-dispersity, and optical properties has been challenging. Here the synthetic challenges associated with InSb CQDs are investigated and it is found that uncontrolled reduction of the antimony precursor hampers the controlled growth of CQDs. To overcome this, a synthetic strategy that combines nonpyrophoric precursors with zinc halide additives is developed. The experimental and computational studies show that zinc halide additives decelerate the reduction of the antimony precursor, facilitating the growth of more uniformly sized CQDs. It is also found that the halide choice provides additional control over the strength of this effect. The resultant CQDs exhibit well-defined excitonic transitions in spectral range of 1.26–0.98 eV, along with strong photoluminescence. By implementing a postsynthesis ligand exchange, colloidally stable inks enabling the fabrication of high-quality CQD films are achieved. The first demonstration of InSb CQD photodetectors is presented reaching 75% external quantum efficiency (QE) at 1200 nm, to the knowledge the highest short-wave infrared (SWIR) QE reported among heavy-metal-free infrared CQD-based devices.

1. Introduction

Infrared (IR) photodetectors enable autonomous driving, augmented reality, biological sensing, and computer vision via light detection and ranging (LiDAR), and hyperspectral imaging technologies.[1] The limited availability of affordable and non-toxic IR active materials hinders their widespread use in this quickly developing consumer electronics market. The III–V semiconductor materials can address some of the prerequisites of high-performance photodetectors, but they face challenges in terms of cost, scalability, and substrate integration. Recent advancements in metamorphic buffers have improved the integration of III–V materials with silicon readout circuits; nevertheless, monolithic integration of III–Vs with silicon remains an ongoing area requiring further maturation.[2] Colloidal quantum dots (CQDs) are a promising low-cost material platform for IR photodetectors. Low-temperature solution processing allows facile integration with silicon and flexible substrates.[3] The quantum confinement of CQD provides an additional advantage of wavelength selectivity and tunability at the material level, reducing the complexity of device structures such as light filtering. PbS and InAs CQD, in particular, are actively investigated for IR light detection applications. Although PbS CQD offer favorable optoelectronic properties and have a well-established material and chemical foundation, their application in consumer products is limited

Muhammad, D. Choi, D. H. Parmar, B. Rehl, Y. Zhang, O. Atan, G. Kim, P. Xia, J. M. Pina, Y. Liu, S. Hoogland, E. H. Sargent
Department of Electrical and Computer Engineering
University of Toronto
10 King's College Road, Toronto, Ontario M5S 3G4, Canada
E-mail: ted.sargent@utoronto.ca

G. Kim
Department of Chemistry
Korea University
Seoul 02841, Republic of Korea

M. Li, Y. Liu
Department of Materials Science and Engineering
University of Toronto
184 College Street, Toronto, Ontario M5S 3E4, Canada

O. Voznyy
Department of Chemistry
University of Toronto
80 St. George Street, Toronto, Ontario M5S 3H6, Canada

due to their high toxicity, resulting in strict regulation.[4] Similarly, tuning the size of InAs CQDs using less toxic, commercially available precursors is challenging.[5]

InSb CQD represent an IR-active materials system of considerable potential interest: it is a direct bandgap semiconductor characterized by a bandgap energy of 0.17 eV at 300 K. The small electron and hole effective masses results in a large exciton Bohr radius of 60 nm. This facilitates greater size-tuning of the bandgap across a significant infrared spectral range, while also preserving quantum confinement effects.

InSb CQD synthesis, though, is challenging and rarely employed as it typically requires pyrophoric and unstable custom antimony precursors.[6] Attempts to synthesize these CQD using more more stable antimony precursors, such as tris(dimethylamido)antimony and $SbCl_3$, have resulted in colloidal dispersions but exhibited worse excitonic absorption features with broad photoluminescence (PL) linewidths.[7–9] Therefore, the development of synthetic strategies that facilitate precise control over the growth of InSb CQD while utilizing stable precursors has become increasingly imperative.

In this study, we developed a synthesis method utilizing a halide-based additive (zinc halides) to achieve superior control over the size distribution of InSb CQD. Density functional theory (DFT) together with experimental results reveal that the addition of the Zn halides saturates the reaction environment and effectively reduces the rate of antimony precursor reduction. These two effects lead to the slowdown of the reaction between the In and Sb precursors that results in the formation of nearly monodispersed CQD, as confirmed by high angle annular dark field scanning transmission electron microscopy (HAADF-STEM). Analysis of optical absorption and transient absorption (TA) spectroscopy reveals well-defined excitonic transitions and strong PL at the band edge, offering tunable optical band gaps from 1.26 to 0.98 eV. We replaced the long aliphatic ligands with smaller halide-based ligands in a two-phase solution-exchange process. This led to an enhancement of the carrier mobility of the CQD in film. We integrated the ligand-exchanged CQD into solid-state films to create functional infrared photodetectors. We report the first demonstration of InSb CQD based photodetectors with external quantum efficiency (EQE) reaching ≈75% at 1200 nm with −1 V bias, exceeding all reported heavy metal-free CQD-based IR photodetectors (see Table S1, Supporting Information).

2. Results and Discussion

The synthesis of InSb CQD is completed in a two-step sequence. First, $InCl_3$ and $SbCl_3$ precursors are solubilized separately in oleylamine (OLA). In the second step, $SbCl_3$-OLA precursor is injected into $InCl_3$-OLA solution, followed by an injection of the reducing agent, alane N,N-dimethylethylamine (DMEDA). Full details of the synthesis method can be found in the Experimental Section and Figure S1 in the Supporting Information.

The InSb CQD sample shows featureless absorption with a long tail at higher wavelength and no emission (**Figure 1**a). Powder X-ray diffraction (PXRD) of the CQD evidences the formation of phase-pure zinc blende InSb CQD (Figures S2, Supporting Information). We attempted to improve size uniformity of the CQD by replacing $InCl_3$ with InCl. Previous studies on InAs

CQD showed that the InCl in the reaction environment helped with size control.[10] But the synthesis of the InSb CQD using InCl precursor shows featureless optical absorption suggesting no control on the nucleation and growth of the CQDs (Figure S3, Supporting Information).

Previous studies on nanocrystals synthesis show that the presence of zinc halides in the reaction environment affect the growth kinetic in various ways including some degree of size control and improve luminescence.[11–14] This motivated us to explore zinc halides as an additive during nucleation and growth of InSb CQD to achieve better monodispersity. Specifically, in our synthetic system, we mixed zinc halide salts with $InCl_3$ and dissolved them in oleylamine followed by sequential injection of $SbCl_3$-OLA and DMEDA. The InSb materials prepared with $ZnCl_2$ exhibited featureless absorption but strong PL appeared (Figure 1a and Figure S4, Supporting Information). This inspired us to explore further the effects of other ZnX_2 salts (X = F, Br, and I). We varied the zinc halides while keeping all other reaction conditions constant (Figure 1a and Figure S4, Supporting Information). The samples prepared using ZnF_2 show a featureless absorption spectrum similar to $ZnCl_2$. In contrast, the samples prepared using $ZnBr_2$ and ZnI_2 exhibit sharper excitonic features and strong luminescence with narrow emission linewidths (Figure 1a and Figure S4, Supporting Information). PXRD analysis evidences the formation of phase-pure material across all the CQD samples (Figure 1b). HAADF-STEM analysis of CQD synthesized with ZnF_2 and $ZnCl_2$ reveals asymmetrical CQD with broad size distributions (Figure S5, Supporting Information). On the other hand, CQD prepared using $ZnBr_2$ and ZnI_2 shows nearly uniform and symmetrical shaped CQDs (Figure S5, Supporting Information).

In InAs synthesis, ZnX_2 were introduced as a way to activate the tris(dimethylamido)arsine precursor, which would not nucleate the CQD otherwise.[15,16] Notably, in our synthesis, as well as in previous work employing different reducing agents, the CQDs easily nucleate even without halide additives.[9] However, the exact role of Zn halides in the synthesis has so far been unclear.[17] We thus turned to DFT modeling to explore the zinc halide effect (see details in the Experimental Section).

Our initial hypothesis was that additional halides provided by Zn or even Zn halide itself can coordinate to Sb and sterically protect it from interacting with DMEDA, and that Br could provide better protection than Cl. DFT simulations revealed, however, that neither the number nor the identity of the halide can prevent the reduction of the Sb halide by AlH_3, which is not just thermodynamically favorable but is also barrierless (we note that including the explicit solvent molecules was critical for facilitating the reduction process) (Figure 1d–f). Similarly, the formation of the $SbCl_3$-$ZnCl_2$ adduct was found to be favorable by only 0.1 eV, insufficient to keep it stable at room temperature, and even in the adduct form providing no additional steric protection against DMEDA.

We noted that $ZnCl_2$ forms a stable adduct with AlH_3 similar to $SbCl_3$ (both formation energies ≈0.8 eV) (Figure 1d,e). However, unlike Sb, Zn does not get reduced, consistent with its higher redox potential. These results suggest that the injected excess $ZnCl_2$ coordinates to the freely available DMEDA, limiting its access and reactivity with $SbCl_3$. Yet again, DFT adduct formation energies show nearly no difference between $ZnCl_2$ and $ZnBr_2$.
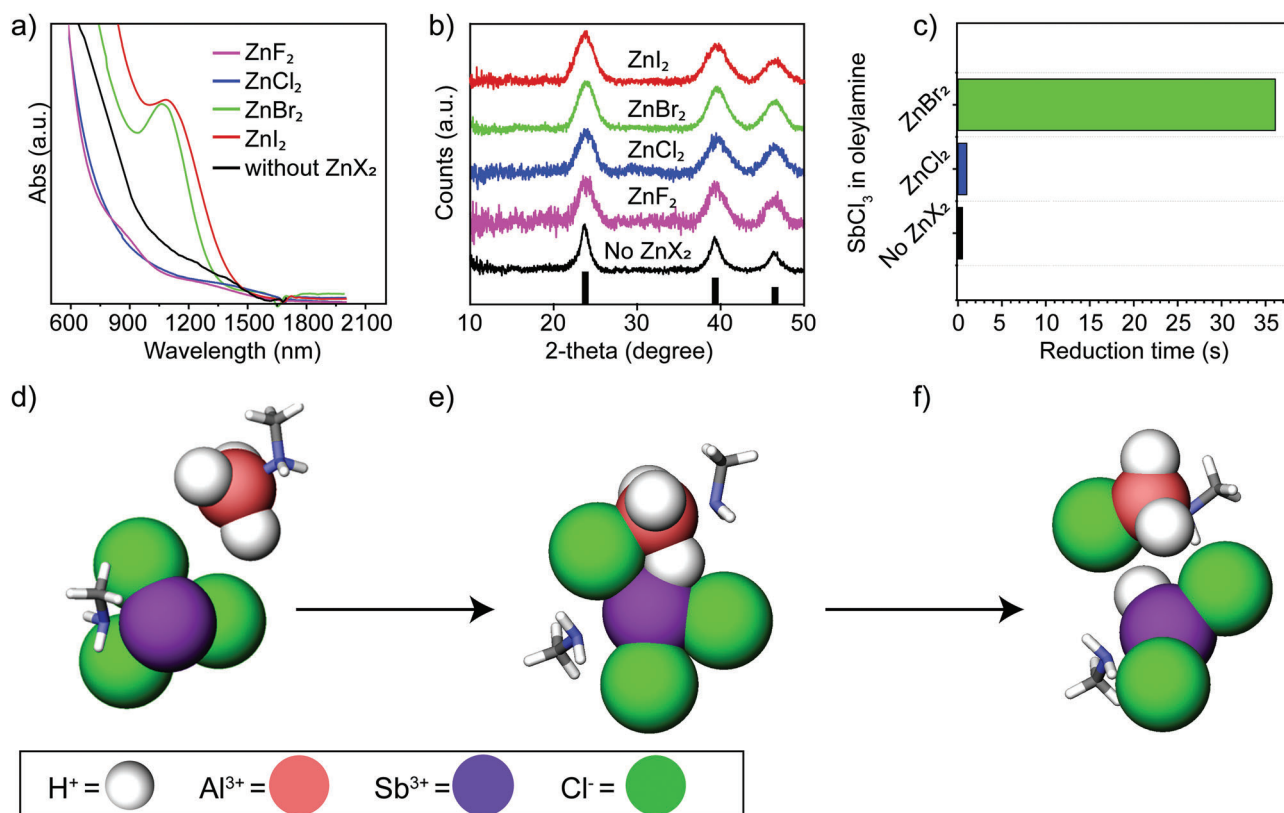
ADVANCED
SCIENCE NEWS
www.advancedsciencenews.com

ADVANCED
MATERIALS
www.advmat.de

Figure 1. Influence of ZnX$_2$ on growth of InSb CQD. a) Optical absorption spectra InSb CQD samples prepared with and without different ZnX$_2$ salts in solution. b) PXRD patterns of corresponding CQD samples recorded by drop casting the samples on silicon substrate. c) Reduction rate of SbCl$_3$ upon DMEDA injection without and with ZnX$_2$. d) DFT simulations of SbCl$_3$ and DMEDA interaction, e) formation of an adduct, with Al lone pair approaching the Cladduct with DMEDA, f) reduced form of SbHCl$_2$ and transfer of Cl to Al, (e) ZnCl$_2$ adduct with DMEDA (some of the coordinating amines are not shown for clarity).

To explain the effect of Cl versus Br one thus needs to turn to their other potential differences. We hypothesized that one such difference could be their solubility in OLA. A less soluble product would need a complexation with DMEDA in order to get solubilized, thus scavenging it more efficiently. Testing this hypothesis with DFT remains unfeasible because to properly capture the weak van der Waals interactions with the long-chain ligands one cannot revert to short-chain amine analogous, substantially increasing the size of the simulation box. Nevertheless, experimental test of ZnX$_2$ solubility in OLA under identical conditions confirmed that ZnCl$_2$ is 1.8 times more soluble then ZnBr$_2$. Moreover, addition of DMEDA improved ZnBr$_2$ solubility, confirming the formation of ZnBr$_2$-DMEDA adduct.

To validate our hypothesis that Zn halide inhibits the reduction of SbCl$_3$, we investigated the reduction rate of SbCl$_3$ precursor alone with and without ZnX$_2$ precursors. All control experiments were performed by fully dissolving SbCl$_3$ precursor in OLA under nitrogen environment. The injection of DMEDA into SbCl$_3$-OLA instantly turns the solution black suggesting the immediate Sb reduction. Similar rate of reduction for SbCl$_3$ was observed when ZnCl$_2$ was added to the solution. Contrary to this, the presence of ZnBr$_2$ in SbCl$_3$ solution exhibits the change in color only after 30 s of DMEDA injection, suggesting significantly lower reduction rate, consistent with the effect of these additives observed on CQD growth. Quantitative comparison of the SbCl$_3$ reduction

with and without ZnX$_2$ is reported in Figure 1c. Notably, neat ZnBr$_2$ solution shows no change in color even after 24 h of injection, suggesting that Zn remains inert against reacting with DMEDA (Figure S6, Supporting Information).

Among various tested ZnX$_2$ salts under comparable synthesis conditions, CQD prepared using ZnBr$_2$ shows narrowest size distribution (Figure S7, Supporting Information). Therefore, the discussion here onward is focused on InSb CQD prepared using ZnBr$_2$ as an additive.

To tune the optical features of InSb CQD, we performed the entire synthesis under an oxygen-free environment using similar methods to those discussed above, which are illustrated in **Figure 2**a. The reaction time was varied from 10 to 45 min while keeping all other synthetic condition fixed. The optical spectroscopy analysis shows that under these conditions, the bandgap of the CQDs can be tuned from 960 to 1270 nm while retaining well-defined excitonic features in their absorption spectrum (Figure 2b). The corresponding emission tunes with the bandgap of the CQDs (Figure S8, Supporting Information) and PL lifetimes increases as the CQD size increases, see Figure S9 in the Supporting Information for PL lifetime traces. Figure 2c shows the well-defined excitonic absorption peak at 1165 nm of a representative sample which is subsequently used for ligand exchanges and devices. The steep absorption edge without a long tail is a sign
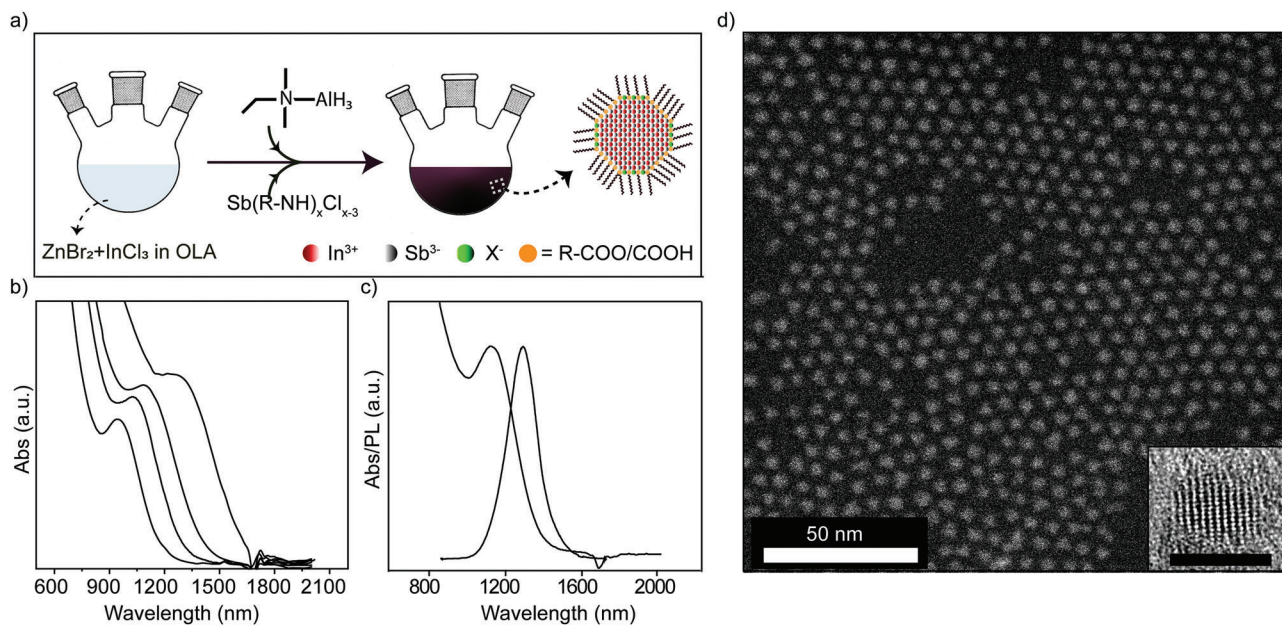
Figure 2. ZnBr$_2$ assisted size-tuning of InSb CQDs. a) Synthesis scheme. b) Size dependent absorption spectra of the InSb CQD. c) Optical absorption (Abs) and photoluminescence (PL) spectra of representative CQD dispersion. d) high angle annular dark field scanning transmission electron microscopy images (HAADF-STEM) of InSb CQD reported in panel (c). High-resolution transmission electron microscopy (HRTEM) image of the CQD is reported as an inset in the same image and the size of the scale bars is 5 nm.

of the highly monodisperse quantum dot ensemble, which we confirmed with HAADF-STEM (Figure 1d and Figure S7, Supporting Information). The PL has a Stokes shift of 120 nm with a peak centered at 1286 nm. The PL spectrum has a full width at half maximum (FWHM) of 136 nm. The PL quantum yield of this CQD batch in solution was 5% ± 2%. We monitored the optical features of these materials over the a 9-week span and found there was no observable change (Figures S10–S12, Supporting Information).

We then turned to deploying these CQDs in the active layer in IR photodetectors. To create high-conductive CQD solids, we developed an in-solution ligand exchange process to remove the bulky, insulating aliphatic ligands for short halide ligands. This process was based on those developed for II–VI and other III–V CQD[18,19] and is described in **Figure 3**a and Figure S13 in the Supporting Information. The synthesized InSb CQD was dispersed in hexane and added to a dimethylformamide (DMF) solution that contained the halide ligands. We found that the DMF solution with just the metal halide ligands (InX$_3$) resulted in nondispersible CQD solids. Using X-ray photoelectron spectroscopy (XPS) we found that the surface of the with metal halide CQD is In rich and therefore forming aggregates due to abundant noncoordinated metal on CQD surface.

We postulated that organic aminohalide ligand could reduce the metallic surface of CQDs. We used a mixture of tetrabutylammonium (TBA) and methylammonium (MA) halides in presence of acetic acid (AA) that enabled the exchanged CQD to be stable in the final solution (Figure 3a,b and Figure S14, Supporting Information). An exchange utilizing only TBA or InX$_3$ resulted in the incomplete removal of the oleate ligands (Figure 3e), resulting in colloidally unstable ink (details in the Experimental Sec-

tion). Addition of AA to the mixture provided acidic hydrogens that facilitated carboxylate removal and results in colloidally stable ink.[20]

Ultrafast pump–probe TA and transient photoluminescence spectroscopy of pristine and ligand exchanged CQD (Figure 3c) were used to study the effect of ligand exchange on the InSb CQD charge carrier dynamics. These transient measurements are suggestive of a trap state density increased following ligand exchange (Figure 3D). While the transient PL of the oleic acid (OA)-capped CQD fit well to a single exponential, indicating charge carriers accumulate at the band edge for radiative recombination, the ligand-exchanged CQDs require a second component to the fit (Figure S15, Supporting Information). With a double-exponential, the OA-capped and ligand-exchanged CQD exhibit a longer component of 90 and 100 ns, respectively, which we assign to radiative recombination. The second, shorter component (≈9 ns), which we attribute to PL decay due to nonradiative recombination, was of larger magnitude for the ligand-exchanged sample. This increase of nonradiative recombination we connect with increased surface traps following the ligand exchange.

The transient absorption spectra, exhibiting bleaches within the steady-state absorbance peaks for both OA-capped and ligand-exchanged CQD, agree in trend with the carrier lifetimes and magnitudes observed using transient PL (Figure 3c). In particular, the bleach dynamics of the ligand-exchanged CQD were more complex than the bleach dynamics of the OA-capped CQD (Figure S15, Supporting Information). Accounting for the band-edge recombination identified from transient PL, we identified two shorter components in the ligand exchanged bleach decay. The first, which was also found in the OA-capped CQD bleach, was of 1–2 ns and we link to nonradiative recombination. The
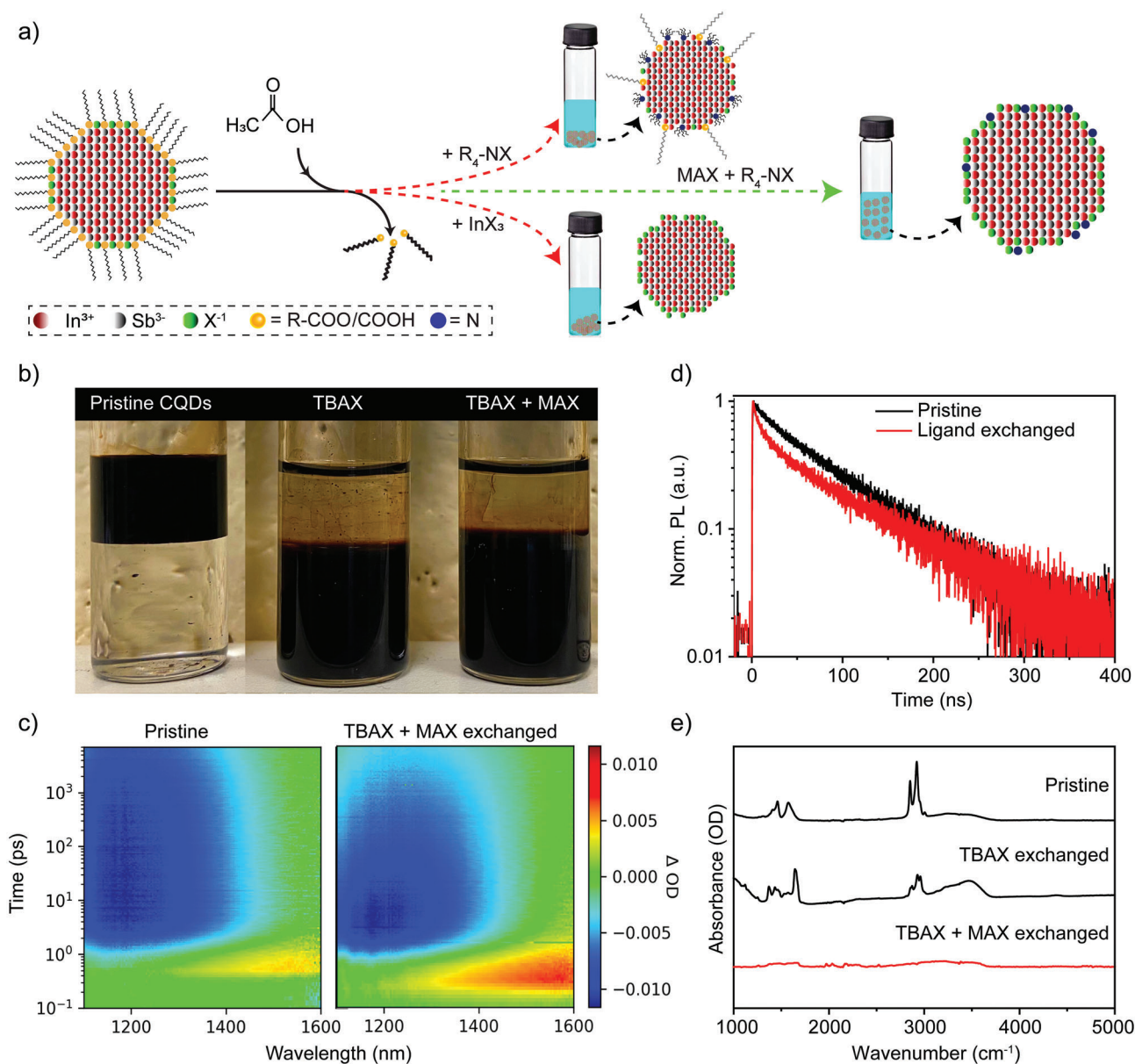
**ADVANCED
SCIENCE NEWS**

www.advancedsciencenews.com

**ADVANCED
MATERIALS**

www.advmat.de

Figure 3. Ligand exchanges and photophysical characterization of the CQD: a) Scheme of the ligand exchange processes. b) Photography of ligand exchanged samples. c) PL decay traces of pristine and ligand exchanged CQD. d) Transient absorption maps of pristine and ligand exchanged CQD after photoexcitation at 800 nm. e) FTIR analysis of the CQD before exchanges, after TBAX, and mixture TBAX plus MAX exchanged treated samples.

second, which was not observed in the OA-capped CQD bleach, was significantly faster (46 ps). We tentatively attribute this fast component to multiexciton generation (MEG) and fast Auger recombination (AR).[21] The appearance of MEG and AR further suggests an increase in trap state postligand exchange. This increase in trap states is highlighted by the increase in magnitude of the two shorter bleach components relative to the OA-capped CQD.

Comparing Fourier-transform infrared spectroscopy (FTIR) spectra (Figure 3e) of the CQD films before and after exchanges with tetrabutylammonium halides (TBAX) reveals substantial decrease in C—H resonances around 2950 cm^{-1} indicating partial substitution of the native ligands. Contrary to this, the use

of TBAX-methylammonium halides (MAX) mixture shows complete removal of the organic ligands in the final ink. The presence of MAX in the ligands exchange solution shifts the equilibrium toward the displacement of organic ligands with halides, resulting in halide passivated CQD. This suggests a single step cascade resurfacing of CQD where acetic acid displace native carboxylate ligands, thereby shifting the equilibrium toward higher binding affinity to halide ligands in polar medium.[20,22,23] Furthermore, we found that the presence of acetic acid during ligand exchange significantly affects the stability of the final ink. The ligand exchanged samples prepared without using acetic acid resulted in CQD aggregation after one week of storage. Nevertheless, the ligand exchange sample prepared in presence of acetic acid remains
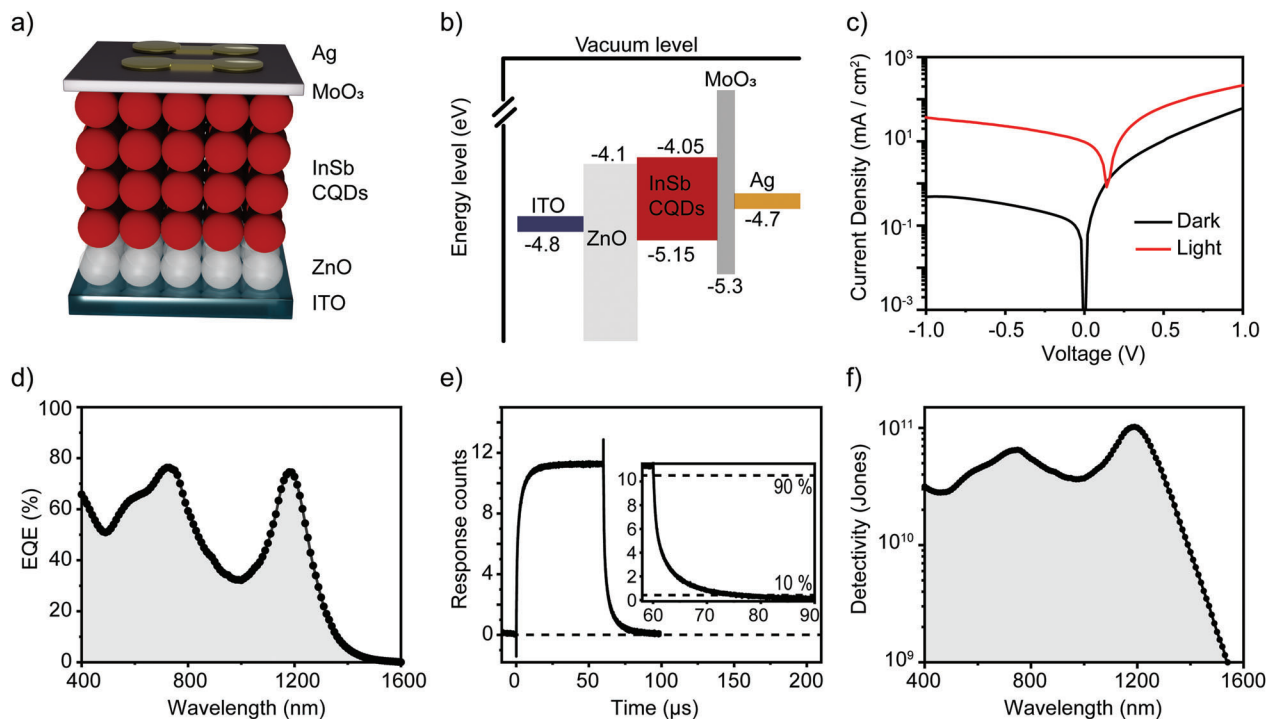
**ADVANCED
SCIENCE NEWS**

www.advancedsciencenews.com

**ADVANCED
MATERIALS**

www.advmat.de

Figure 4. InSb CQD based IR photodetectors performance. a,b) Scheme showing the device architecture used in InSb photodetectors devices and the band alignment of layers. c) Dark and illuminated *J–V* characteristics of InSb photodetector. The Table S2 in the Supporting Information shows summary of dark current, current density, open circuit voltage, and rectification ratio. d) EQE (1 V) and e) transient photocurrent and f) detectivity of InSb CQD photodetector.

stable after multiple cycles of washing and retain optical features upon storage. This is likely due to acetic acid assisted protonation of halide ligands which facilitates the colloidal stability of the ink.[24] The proposed ligand exchange mechanism is detailed in Figure S14 in the Supporting Information.

PXRD analysis of the CQD after ligand exchange shows phase pure zinc blend InSb CQD (Figure S16, Supporting Information), indicating that the inorganic core of the CQD remains intact during resurfacing. XPS analysis of the pristine and ligand exchanged CQD shows significant decrease in the O1s peak, and reduction of the InSb ($3d_{5/2}$) peak width (Figures S17 and S18, Supporting Information), implying the clean CQD surface. Elemental analysis via XPS revealed that, upon exchange, the In:Sb ratio decreased from 2.1 to 1.6 indicating the removal of surface indium atoms. This observation is consistent with previous reports describing postligand exchange reconstruction of III–V CQD surfaces.[18] A higher In/Sb ratio in the initial sample (before ligand exchanges) may result from indium halide-rich CQD surfaces and/or residual indium-organic complexes.

InSb photodetectors are fabricated using the structure of **Figure 4**a. ZnO nanoparticles are deposited on an indium tin oxide (ITO) substrate, followed by the deposition of the ligand-exchanged InSb CQDs. Molybdenum oxide (MoOx) is then thermally evaporated onto the InSb CQD active layer. The structure is completed with Ag deposition to form the photodetector top contact. Previous studies on III–V CQDs photodetectors shows that using an Au electrode (instead of Ag) did not lead to improved performance, despite Au's deeper work function.[25,26] This is likely due to better energy alignment between the Ag work

function and the conducting intra-band states in MoOx. Additionally, due to its cost-effectiveness compared to Au, we opted to utilize Ag consistently in the present study. Alternative device structures were explored but resulted in poor diode behavior and high dark currents (Figure S20 and Table S3, Supporting Information). Future studies could seek to enhance band alignment and charge extraction mechanisms in InSb CQD devices.

Ultraviolet photoelectron spectroscopy shows that valence band of ligand exchanged QD films shifted toward vacuum compared to the pristine CQD (Figure S21, Supporting Information). The band alignment of the overall device architecture used in this study is reported in Figure 4b. Although the MoO$_3$ layer has an energy potential difference of ≈0.15 eV with the valence band of the CQD active layer, it efficiently blocks electron back injection, successfully lowering the dark current compared to the control devices prepared without using MoO$_3$ blocking layer. This result in dark current of 0.48 mA cm^{-2} at 1.0 V reverse bias (Figure 4c).

The EQE of the InSb device presented in Figure 4d demonstrated a remarkable value of 74.4% under 1 V bias. We then investigated the photodetector's transient photocurrent responses (Figure 4e). The photodetector shows a rise and fall times (from 10% to 90% and 90% to 10% of the normalized photocurrent) of 7.3 and 5.4 µs, respectively. We measured a specific detectivity (based on noise current) of 10^{11} Jones (5–50 kHz) at 1200 nm (Figure S23, Supporting Information). We studied the stability of InSb CQD photodetector devices before and after encapsulation in ambient air. Nonencapsulated devices showed high instability under ambient conditions. UV-resin encapsulation

**ADVANCED
SCIENCE NEWS**

www.advancedsciencenews.com

**ADVANCED
MATERIALS**

www.advmat.de

improved stability, but prolonged exposure led to changes in current density-voltage characteristics—increased leakage, and smaller J_{sc} value due to oxidation of InSb CQDs. This suggests that the current UV-resin encapsulation method may not be entirely effective in safeguarding the devices and highlights the need for more effective encapsulation strategies due to the sensitiveness of the InSb CQDs to air.

In conclusion, we report here a synthetic strategy to prepare nearly monodisperse InSb CQD combining off-the-shelf nonpyrophoric precursors together with various zinc halides additives. Combined experimental and computational studies shows that ZnX$_2$ slows down the reduction of SbCl$_3$. The improved control over the antimony precursor during nucleation and growth enables the synthesis of monodisperse CQD. A postsynthetic surface treatment based on MAX:TBAX and acetic acid results in complete displacement of the native long chain organic ligands and the formation of CQD solids. This enabled us to fabricate a highly efficient InSb-based photodetector, achieving a detectivity of 1.02×10^{11} Jones and EQE of 75% at 1200 nm, a record among all reported lead free CQD based photodetectors.

3. Experimental Section

Materials: Indium chloride (InCl$_3$, 99.99%), Oleic acid (OA, 99%), Oleylamine (OLAM, 98%), *N*,*N*-dimethylformamide (DMF, 99.8% anhydrous), alane *N*,*N*-dimethylethylamine complex solution (DMEDA, 0.5 M toluene), zinc chloride (ZnCl$_2$, >98%), zinc bromide (ZnBr$_2$, 99.999%), octane (99% anhydrous), acetonitrile (ACN, 99.8% anhydrous), toluene (Tol, 99.8% anhydrous), Methylammonium chloride (MACl, 99%), Tetrabutylammonium bromide (TBABr, 99%), and Tetrabutylammonium iodide (TBAI, 99%) were purchased from sigma. Indium (III) bromide (InBr$_3$, 99.999% anhydrous) and antimony(III) chloride (99%) were purchased from Strem Chemicals, Inc. Zinc fluoride (ZnF$_2$, anhydrous) and zinc iodide (ZnI$_2$, 98%) were purchased from fisher scientific. All the mentioned chemicals were used as received.

InSb Colloidal Quantum Dot Synthesis: A solution mixture of 1 mmol of InCl$_3$, 2.85 mmol of ZnX$_2$, and 35 mL of OLAM was added in a 250 mL flask while stirring and kept under a vacuum at 120 °C for 3 h. After that, the reaction mixture is cool down to 50 °C followed by a sequential injection of 1.3 mL SbCl$_3$-OLAM (separately prepared by dissolving in 285 mg of SbCl$_3$ in 5 mL of predried OLAM) and 5 mL alane *N*,*N*-dimethylethylamine (5 mL). Subsequently, the reaction temperature is increased to 260 °C and maintained for desired time (15–45 min). Then, the reaction flask is allowed to cool down to room temperature and CQDs are precipitated using acetonitrile as an antisolvent followed by their redispersion in toluene. Detailed steps for initial ligand exchanges and washing of CQDs are provided in the Supporting Information.

Control experiments for the reduction of SbCl$_3$, with and without ZnX$_2$, were conducted in a completely oxygen-free environment, employing methods similar to those used in the synthesis of CQDs.

Solution Phase Ligand Exchanges: The solution phase ligand exchange process for InSb CQD was performed under ambient conditions. The pristine InSb CQD, with native OA ligands, was dispersed in an anhydrous hexane solvent with a concentration of ≈50 mg mL^{-1}. A ligand exchange solution was prepared by dissolving a halide source compound in 5 mL of DMF in a molar ratio of 1:5(0.5):5:0.15, where each ratio represents MACl:TBABr(MABr):TBAI:AA, respectively. Note that AA (≈10 µL, 0.15 mmol) was added after dissolving all the halide compounds in DMF to prevent side reactions. Then 0.3–0.6 mL of OA-capped InSb CQD in hexane was vigorously mixed with 0.6–1.2 mL of the ligand exchange solution for 2 min using a vortex. Once the InSb CQD was transferred to the DMF phase, the transparent organic layer was removed, followed by adding 1 mL of fresh anhydrous hexane to the DMF phase for washing.

This process was repeated twice to remove organic residue from the final ink. The halide capped InSb CQD in the DMF phase was precipitated by adding anhydrous toluene and hexane. The pellet was then redispersed in pure DMF and precipitated once more to remove any TBA or MA residual in the DMF phase. Finally, the precipitate was dried completely and redispersed in a DMF:ACN (1:3, v/v) solvent mixture with a concentration of ≈300 mg mL^{-1} to create an InSb CQD ink. The ink was centrifuged at 14 000 rpm for 2 min just before the film deposition process. It was sought to simplify the materials processing protocol by removing one of the halide sources (either TBAX or MAX). This change resulted in 1) aggregation of CQDs at the interface of solvent mixture during the two-phase ligand exchange and 2) less dispersible CQDs following the ligand exchange reaction. Similarly, the addition of InX$_3$ during ligand exchange reaction was found to be detrimental to ink stability of CQDs. In contrast, use of the mixture of TBAX and MAX results in a stable ink. It was believed that both have a role to play: MAX is a primary ammonium and thus more acidic, which is shown to help with stripping off the original ligand. TBAX is more bulky, which may help with colloidal stability.

Device Fabrication: The ITO glass substrate was thoroughly cleaned using sonication with deionized water, acetone, and isopropanol, each for 30 min. For the ZnO layer, presynthesized ZnO nanoparticles at a concentration of 80 mg mL^{-1} were spin-coated twice onto the substrate at 5000 rpm for 30 s. The active layer was deposited in the glove box on top of the ZnO layer using 35 µL of InSb ink, utilizing a two-step spin-coating process consisting of 1000 rpm for 20 s followed by 1500 rpm for 30 s. Finally, the device was completed by thermal deposition of a 10 nm MoO$_3$ layer and a 140 nm silver electrode layer onto the active layer. All device measurements are done under ambient air at room temperature.

Characterization of CQD and Devices: *FTIR Spectroscopy*: The FTIR measurements were carried out using the Thermo Scientific iS50 instrument, covering the spectral range from 8000 to 350 cm^{-1} with a resolution of 4 cm^{-1}. The measurements were performed in attenuated total reflection configuration.

Transient Absorption Measurements: The 5 kHz repetition rate femtosecond laser pulses were generated using a regeneratively amplified ytterbium-doped potassium gadolinium tungstate(Yb:KGW) laser (PHAROS, Light Conversion) with a 1030 nm fundamental wavelength. The fundamental was used to produce a pump beam at 400 nm with an optical parametric amplifier (ORPHEUS, Light Conversion). Then, the pump and fundamental were aligned into a commercial transient absorption spectrometer (Helios, Ultrafast). To generate the white continuum probe, the fundamental through a delay stage is focused into a sapphire crystal. The pump beam repetition rate is controlled by a mechanical chopper, reducing its repetition rate to 2.5 kHz. The TA measurements were performed using an average power of 1 µW with a spot size of 0.4 µm^2.

Device Current–Voltage Characterization: Keithley 2400 source meter is used for current–voltage measurements, scanned from −1 to +1 V in 0.02 V steps without interval delay time.

Device Response Time Measurement: The time response of the InSb device was measured using a 1 GHz oscilloscope (DSO8104A Infinium, Agilent). A 1310 nm diode laser (Thorlabs ML725B8F) connected to a function generator (Agilent 33220A) to modulate 10 kHz was used as an illumination source. The Femto DHPCA-100 preamplifier at 10^3 V A^{-1} was used for photodetector signal amplification.

PL Characterization: Steady-state PL was measured by a Horiba Fluorolog system with a monochromatized Xe lamp as the excitation source. To acquire transient PL, a time-correlated single photon counting detector and a pulsed near infrared laser diode (DD-830L, DeltaDiode, 820 nm, HORIBA Scientific) were used. The sample was illuminated 15° with respect to the surface normal. The photoluminescence was collected at 75° with respect to the surface normal and measured with a iHR320 spectrometer (HORIBA Scientific, 600 grooves mm^{-1}, 1000 nm blaze wavelength) and InGaAs photodetector (S1-H10330-75).

PL Quantum Yield Measurements: The measurements were performed by using a Quanta-Phi integrating sphere of the Fluorolog system. Prior to the measurements, the detector was calibrated for spectral variance with a Newport white light source to ensure accurate values.

TA Measurements: A regeneratively amplified Yb:KGW laser (PHAROS, Light Conversion) was used to generate femtosecond laser pulses (1030 nm, 5 KHz repetition rate, ≈200 fs). The majority of the beam power was used to pump an optical parametric amplifier (ORPHEUS, Light Conversion) to generate the pump laser (FWHM ≈10 nm) which was passed through a chopper (pump repetition = 2.5 KHz). The remaining portion of the 1030 nm beam was passed through a delay stage and focused through a sapphire crystal to generate a white light continuum probe in the NIR. The pump and probe beams were focused spatially and temporally through the sample at an angle of ≈30° with respect to each other. The remaining probe light was directed into a commercial transient absorption spectrometer (Helios, Ultrafast Systems, InGaAs 256 pixels). Sample measurement was obtained with a pump power of 1000 μW.

PXRD Measurements: PXRD measurements were conducted using a Rigaku MiniFlex 600 diffractometer (Bragg-Brentano geometry) equipped with a NaI scintillation counter detector and a monochromatized Cu K_α radiation source ($\lambda = 1.5406$ Å) operating at a voltage of 40 kV and current of 15 mA.

Transmission Electron Microscopy (TEM) Characterization: Bright-field TEM, high-resolution TEM, and STEM-HAADF images of the QD samples were acquired using a Hitachi HF-3300 transmission electron microscope operating at an accelerating voltage of 300 kV. The samples were prepared by drop casting diluted solutions of NCs onto carbon-coated 200 mesh copper grids.

High-Resolution TEM and Energy Dispersive X-Ray Spectroscopy: The characterization was performed by using a JEOL JEM2200 image-corrected instrument operated at 200 kV and equipped with an in-column Omega energy filter and Bruker Quantax 400 Energy-dispersive X-ray spectroscopy (EDX) system with a 60 mm^2 XFlash detector. Partial high-resolution transmission electron microscopy (HRTEM) and EDX characterization were taken on a ThermoFisher Scientific Titan Cubed Themis G2 300 transmission electron microscope with an acceleration voltage of 300 kV and equipped with a Super-X4 probe super energy spectrum.

External Quantum Efficiency Measurement: The EQE of InSb devices were measured with EnlinTech QE-R Quantum Efficiency Analyzer, 400–1700 nm, resolution 10 nm, monochromatic light chopped mechanically in 210 Hz.

DFT Calculations: Calculations were performed in CP2K suite,[27] using Goedecker-Tetter Hutter pseudopotentials,[28] generalized gradient approximation with Perdew–Burke–Ernzerhoff functional,[29] and DZVP basis set optimized for molecules.[30]

Methylamine was used instead of oleylamine to minimize the number of atoms in simulations and minimize the degrees of freedom to avoid energy fluctuations. Similarly, dimethylethylamine on the alane was replaced by the methylamine, anticipating an easy exchange of the amine ligand in the neat amine solvent solution. Molecular dynamics simulations were performed to test how metal halides dissolve in amines and then representative geometries were used in Sb-halide-alane interactions. It is found that the precursors in OLA do not dissociate into ions (Sb^{3+}, Zn^{2+}, Cl^-) completely and cations remain coordinated to halides. A loss or gain of one halide ion is in principle possible, resulting in charged complexes, e.g., $SbCl_4^-$ and $ZnCl^+$, in addition to the more abundant $SbCl_3$ and $ZnCl_2$ coordinated by amines.

Configurations with two, three, and four halides around Sb as well as with full $ZnCl_2$ molecule attached to $SbCl_3$ all failed to explain the reduction process by AlH_3. Even though without the explicit solvent it was possible to block the reduction, the energetics of the reaction would completely change when explicit amines were included. In addition, amine hydrogens would coordinate to the halide and further facilitate barrierless transfer of H from Al to Sb and Cl from Sb to Al.

Supporting Information

Supporting Information is available from the Wiley Online Library or from the author.

Conflict of Interest

The authors declare no conflict of interest.

Data Availability Statement

The data that support the findings of this study are available from the corresponding author upon reasonable request.

[1] F. P. García De Arquer, D. V. Talapin, V. I. Klimov, Y. Arakawa, M. Bayer, E. H. Sargent, *Science* **2021**, *373*, eaaz8541.

[2] A. Rogalski, P. Martyniuk, M. Kopytko, P. Madejczyk, S. Krishna, *Sensors* **2020**, *20*, 7047.

[3] X. Xiao, K. Xu, M. Yin, Y. Qiu, W. Zhou, L. Zheng, X. Cheng, Y. Yu, Z. Ning, *Appl. Phys. Lett.* **2020**, *116*, 101102.

[4] M. W. Neathery, W. J. Miller, *J. Dairy Sci.* **1975**, *58*, 1767.

[5] T. Kim, D. Shin, M. Kim, H. Kim, E. Cho, M. Choi, J. Kim, E. Jang, S. Jeong, *ACS Energy Lett.* **2022**, *8*, 447.

[6] W. Liu, A. Y. Chang, R. D. Schaller, D. V. Talapin, *J. Am. Chem. Soc.* **2012**, *134*, 20258.

[7] V. Srivastava, E. Dunietz, V. Kamysbayev, J. S. Anderson, D. V. Talapin, *Chem. Mater.* **2018**, *30*, 3623.

[8] S. Busatto, M. De Ruiter, J. T. B. H. Jastrzebski, W. Albrecht, V. Pinchetti, S. Brovelli, S. Bals, M.-E. Moret, C. De Mello Donega, *ACS Nano* **2020**, *14*, 13146.

[9] T. Zhao, N. Oh, D. Jishkariani, M. Zhang, H. Wang, N. Li, J. D. Lee, C. Zeng, M. Muduli, H.-J. Choi, D. Su, C. B. Murray, C. R. Kagan, *J. Am. Chem. Soc.* **2019**, *141*, 15145.

[10] M. Ginterseder, D. Franke, C. F. Perkinson, L. Wang, E. C. Hansen, M. G. Bawendi, *J. Am. Chem. Soc.* **2020**, *142*, 4088.

[11] S. Ghosh, L. Manna, *Chem. Rev.* **2018**, *118*, 7804.

[12] H. Li, W. Zhang, Y. Bian, T. K. Ahn, H. Shen, B. Ji, *Nano Lett.* **2022**, *22*, 4067.

[13] W.-S. Song, H.-S. Lee, J. C. Lee, D. S. Jang, Y. Choi, M. Choi, H. Yang, *J Nanopart Res* **2013**, *15*, 1.

[14] J. J. Calvin, J. K. Swabeck, A. B. Sedlak, Y. Kim, E. Jang, A. P. Alivisatos, *J. Am. Chem. Soc.* **2020**, *142*, 18897.

[15] V. Grigel, D. Dupont, K. De Nolf, Z. Hens, M. D. Tessier, *J. Am. Chem. Soc.* **2016**, *138*, 13485.

[16] R. Tietze, R. Panzer, T. Starzynski, C. Guhrenz, F. Frenzel, C. Würth, U. Resch-Genger, J. Weigand, A. Eychmülle, *Part. Part. Syst. Charact.* **2018**, *35*, 1800175.

[17] D. Zhu, F. Bellato, H. Bahmani Jalali, F. Di Stasio, M. Prato, Y. P. Ivanov, G. Divitini, I. Infante, L. De Trizio, L. Manna, *J. Am. Chem. Soc.* **2022**, *144*, 10515.

[18] M.-J. Choi, L. K. Sagar, B. Sun, M. Biondi, S. Lee, A. M. Najjariyan, L. Levina, F. P. García de Arquer, E. H. Sargent, *Nano Lett* **2021**, *21*, 6057.

[19] Z. Yang, J. Z. Fan, A. H. Proppe, F. P. G. D. Arquer, D. Rossouw, O. Voznyy, X. Lan, M. Liu, G. Walters, R. Quintero-Bermudez, B. Sun, S. Hoogland, G. A. Botton, S. O. Kelley, E. H. Sargent, *Nat. Commun.* **2017**, *8*, 1325.

[20] D. M. Balazs, D. N. Dirin, H.-H. Fang, L. Protesescu, G. H. Ten Brink, B. J. Kooi, M. V. Kovalenko, M. A. Loi, *ACS Nano* **2015**, *9*, 11951.

[21] A. Y. Chang, W. Liu, D. V. Talapin, R. D. Schaller, *ACS Nano* **2014**, *8*, 8513.

[22] M.-J. Choi, F. P. García De Arquer, A. H. Proppe, A. Seifitokaldani, J. Choi, J. Kim, S.e-W. Baek, M. Liu, B. Sun, M. Biondi, B. Scheffel, G. Walters, D.-H. Nam, J. W. Jo, O. Ouellette, O. Voznyy, S. Hoogland, S. O. Kelley, Y. S. Jung, E. H. Sargent, *Nat. Commun.* **2020**, *11*, 103.

[23] H. You, W. Wang, S. Yang, *ACS Appl. Mater. Interfaces* **2014**, *6*, 19035.

[24] J. Owen, *Science* **2015**, *347*, 615.

[25] B. Sun, A. M. Najarian, L. K. Sagar, M. Biondi, M.-J. Choi, X. Li, L. Levina, S.e-W. Baek, C. Zheng, S. Lee, A. R. Kirmani, R. Sabatini, J. Abed, M. Liu, M. Vafaie, P. Li, L. J. Richter, O. Voznyy, M. Chekini, Z.-H. Lu, F. P. García De Arquer, E. H. Sargent, *Adv. Mater.* **2022**, *34*, 2203039.

[26] P. Xia, B. Sun, M. Biondi, J. Xu, O. Atan, M. Imran, Y. Hassan, Y. Liu, J. M. Pina, A. M. Najarian, L. Grater, K. Bertens, L. K. Sagar, H. Anwar, M.-J. Choi, Y. Zhang, M. Hasham, F. P. García De Arquer, S. Hoogland, M. W. B. Wilson, E. H. Sargent, *Adv. Mater.* **2023**, *35*, 2301842.

[27] J. Vandevondele, M. Krack, F. Mohamed, M. Parrinello, T. Chassaing, J. Hutter, *Comput. Phys. Commun.* **2005**, *167*, 103.

[28] S. Goedecker, M. Teter, J. Hutter, *Phys. Rev. B* **1996**, *54*, 1703.

[29] J. P. Perdew, K. Burke, M. Ernzerhof, *Phys. Rev. Lett.* **1996**, *77*, 3865.

[30] J. VandeVondele, J. Hutter, *J. Chem. Phys.* **2007**, *127*, 114105.